madSTORM: a superresolution technique for large-scale multiplexing at single-molecule accuracy

Jason Yi[a], Asit Manna[a], Valarie A. Barr[a], Jennifer Hong[b], Keir C. Neuman[b], and Lawrence E. Samelson[a,*]

[a]Laboratory of Cellular and Molecular Biology, National Cancer Institute, and [b]Laboratory of Single Molecule Biophysics, National Heart, Lung, and Blood Institute, National Institutes of Health, Bethesda, MD 20892

ABSTRACT **Investigation of heterogeneous cellular structures using single-molecule localization microscopy has been limited by poorly defined localization accuracy and inadequate multiplexing capacity. Using fluorescent nanodiamonds as fiducial markers, we define and achieve localization precision required for single-molecule accuracy in dSTORM images. Coupled with this advance, our new multiplexing strategy, madSTORM, allows accurate targeting of multiple molecules using sequential binding and elution of fluorescent antibodies. madSTORM is used on an activated T-cell to localize 25 epitopes, 14 of which are on components of the same multimolecular T-cell receptor complex. We obtain an average localization precision of 2.6 nm, alignment error of 2.0 nm, and <0.01% cross-talk. Combining these technical advances affords the ability to move beyond obtaining superresolved structures to defining spatial relationships among constituent molecules within structures. Probing the molecular topology of complex signaling cascades and other heterogeneous networks is feasible with madSTORM.**

Monitoring Editor
Jennifer Lippincott-Schwartz
Howard Hughes Medical Institute

Received: May 25, 2016
Revised: Aug 2, 2016
Accepted: Sep 27, 2016

INTRODUCTION

Localization precision in direct stochastic optical reconstruction microscopy

A variety of superresolution microscopy techniques have been developed to overcome the diffraction limit of light microscopy (~200 nm). Among these is a category of techniques called single-molecule localization microscopy (SMLM), which includes photoactivation localization microscopy (PALM) and stochastic optical reconstruction microscopy (STORM). SMLM techniques share in the use of fluorophores that can be switched between on (fluorescent) and off (dark/photoswitched) states, allowing sequential localization of fluorescence from single molecules (Betzig *et al.*, 2006; Hess *et al.*, 2006; Rust *et al.*, 2006).

Owing to its compatibility with commercially available dyes and microscopes, direct STORM (dSTORM) has become a widely adopted SMLM technique (van de Linde *et al.*, 2011). dSTORM has been used for two purposes: visualizing structures at high resolution (requires high labeling density) and accurately locating single-molecule positions (requires high precision). Regarding the first purpose, a recent study showed that even at maximum labeling density of fluorescent antibody molecules, discontinuous patterns are observed along bundled actin filaments (Kiuchi *et al.*, 2015), making it difficult to reach nanoscale resolution as defined by the Nyquist criterion. Furthermore, a separate study showed that five times the labeling density as calculated by the Nyquist criterion is required to properly resolve nanostructures such as F-actin (Legant *et al.*, 2016). Because antibody-based SMLM techniques cannot achieve sufficient labeling density required for highly resolved visualization of structures, we used madSTORM for the second purpose: to locate multiple antibody positions each at single-molecule accuracy.

dSTORM can routinely achieve ~10-nm localization precision, defined as the uncertainty in calculating the center of a diffraction-limited point spread function (PSF). However, despite the high precision estimated using localization algorithms (Thompson *et al.*, 2002; Mortensen *et al.*, 2010; Rieger and Stallinga, 2014), accurate determination of the actual location of single molecules has been hampered by a number of issues. First, mechanical movement of the microscope

This article was published online ahead of print in MBoC in Press (http://www.molbiolcell.org/cgi/doi/10.1091/mbc.E16-05-0330) on October 5, 2016.

*Address correspondence to: Lawrence Samelson (samelsonl@mail.nih.gov).

Abbreviations used: AFC, averaged fiducial correction; FND, fluorescent nanodiamond; SMLM, single-molecule localization microscopy; STORM, stochastic optical reconstruction microscopy; TCR, T-cell receptor.

stage during image acquisition adds significant uncertainty to localization precision. Second, although SMLM images are often perceived to be point patterns of single-molecule positions, the distribution of successive localizations is fourfold to sixfold broader than the calculated precision of individual localizations. Thus, for densely labeled samples, we show that the precision level of 5–10 nm currently achieved using dSTORM dyes (Dempsey *et al.*, 2011) is not sufficient to locate single molecules with a high degree of confidence.

Multiplexed superresolution imaging

In addition to the diffraction limit, light microscopy is further restricted by spectral limits. Simultaneous visualization of multiple targets requires fluorescent probes with nonoverlapping spectral profiles, generally restricting fluorescence-based light microscopy to six colors and SMLM to two or three colors (Bates *et al.*, 2007; Dempsey *et al.*, 2011; van de Linde *et al.*, 2011). Moreover, nonlinear chromatic aberration causes misalignment of multicolor images (Pertsinidis *et al.*, 2010; Erdelyi *et al.*, 2013). To overcome these limits, previous studies imaged multiple targets using repetitive photobleaching or chemical quenching of sequentially bound fluorophores (Schubert *et al.*, 2006; Nanguneri *et al.*, 2012; Gerdes *et al.*, 2013; Jungmann *et al.*, 2014; Tam *et al.*, 2014; Valley *et al.*, 2015). Although these methods can overcome the spectral limits of microscopy, fluorescence bleaching is known to be a toxic process (Hoebe *et al.*, 2007), and prolonged bleaching or quenching may cause unwanted side effects such as reverse cross-linking and denaturation of proteins. Furthermore, the accumulation of fluorescent probes could lead to steric blocking of binding sites in the sample, preventing large-scale multiplexing and robust targeting of epitopes. To avoid such steric interference, a recent study achieved multiplexing using stochastic exchange of freely diffusing protein fragments (Kiuchi *et al.*, 2015). Although this method allows dense labeling of cellular structures, it requires extensive biochemical preparation to isolate peptide fragments, cannot locate single-molecule positions, and does not readily facilitate large-scale multiplexing using commercially available probes.

T-cell receptor microclusters

Engagement of the T-cell receptor (TCR) leads to rapid recruitment of TCR microclusters at the site of activation (Bunnell *et al.*, 2002; Campi *et al.*, 2005). Organelles and cytoskeletal structures are subsequently polarized, and a highly ordered structure, the immunological synapse, forms over time (Kaizuka *et al.*, 2007; Yi *et al.*, 2012, 2013). Although TCR microclusters have been studied extensively using conventional light microscopy techniques, their nanostructure and the relative distribution of molecular components are not well characterized due to the diffraction and spectral limits of light microscopy.

We showed using two-color PALM that distinct molecular patterns can be observed in TCR microclusters (Sherman *et al.*, 2011). However, PALM is not amenable to visualization of the numerous molecules involved in TCR signaling. Moreover, we and others observed artificial clustering of fluorescently tagged molecules, in particular those tagged with PA-mCherry (Wang *et al.*, 2014; unpublished data), leading us to seek new imaging modalities in visualizing the immunological synapse.

In this study, we use fluorescent nanodiamonds as fiducial markers to precisely register samples for drift correction and alignment, define the necessary localization precision required for robust detection of single antibody molecules, and describe a novel strategy that expands the multiplexing capacity of dSTORM. Using this precise, multiplexed dSTORM technique, we probe the nanoscale topography of molecules involved in the TCR signaling cascade near the activated surface of a T-cell.

RESULTS

Fluorescent nanodiamond fiducial markers

Because SMLM images are obtained over thousands of time-lapse frames, nanoscale movements of the microscope stage can significantly compromise the precision of the final superresolution image (Pertsinidis *et al.*, 2013). To compensate for stage movement during image acquisition, stage drift is commonly estimated from regression-based fitting of binned localizations from the image itself (cross-correlation) or sequential localizations from fiducial markers (fiducial correction; Betzig *et al.*, 2006; Bates *et al.*, 2013). However, these methods require optimization of multiple parameters for each image stack and cannot account for stage movements at short time scales (e.g., mechanical vibration). Rather than correcting stage movement after image acquisition, a few studies used hardware-based strategies to stabilize the stage in real time (Pertsinidis *et al.*, 2010). However, they require complicated hardware and software modifications, making them difficult to implement.

An alternative to regression-based drift correction methods is averaged fiducial correction (AFC), in which change in the centroid position of multiple fiducial markers is subtracted from all localizations per frame (Rust *et al.*, 2006; see *Materials and Methods*). This method does not require optimization of parameters and is sensitive to rapid stage movements (see later discussion). However, because AFC requires multiple fiducial markers to be detected in every image frame, we sought to identify a sufficiently photostable fiducial marker. After 4000 acquisitions at 100 ms/frame excited with a 647-nm laser (100 mW), fluorescent beads (100 nm TetraSpeck; Invitrogen, Carlsbad, CA) were completely photobleached, showing them to be incompatible with long-term AFC (Figure 1A). Conversely, at the same acquisition setting, gold nanorods (25 × 550 nm; Nanopartz, Loveland, CO) displayed random spikes in emission that saturated the dynamic range of the electron-multiplying (EM) camera, restricting their localization in a number of image frames. Finally, we tested negatively charged, nitrogen-vacancy-center fluorescent nanodiamonds (FNDs; 100 nm; Adamas, Raleigh, NC), which are ideal fiducial markers for SMLM because they are small and bright and display a broad spectral range of fluorescence (Bumb *et al.*, 2013). Compared to fluorescent beads and nanogold particles, emission from FNDs was stable over time (Figure 1A), resulting in better localization precision and drift correction (Supplemental Figure S1).

Using FNDs embedded on a poly-L-lysine (PLL)–coated coverslip, we compared the relative performance of cross-correlation, fiducial correction, and AFC. In particular, we tested for their ability to correct rapid stage movements in images acquired on a microscope vibrating due to an imbalanced air-table. We also note that drift correction was independently measured using a set of FNDs not included in the drift correction process. Whereas cross-correlation and fiducial correction could compensate for the overall stage drift, they could not correct the rapid vibrations, resulting in an asymmetry in the distribution of FND localizations in the direction of the vibration (30,000 frames; Figure 1, B, C, and I). In contrast, application of AFC to the same FNDs yielded a symmetric distribution of localizations (Figure 1, D and I). Furthermore, the variance in the localization distribution was smaller with AFC than with other correction methods, evident from three-dimensional (3D) histogram plots (Figure 1, E–G) and their SDs (Table 1).

SMLM studies have assumed that the localization precision calculated using various PSF fitting algorithms (Thompson *et al.*, 2002; Mortensen *et al.*, 2010; Rieger and Stallinga, 2014) corresponds to

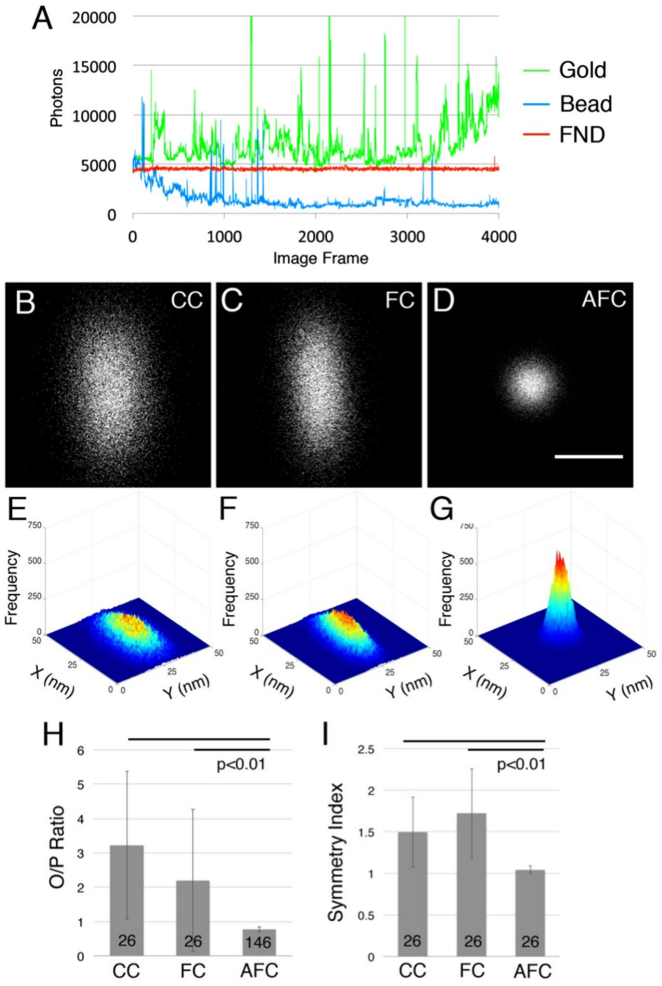

FIGURE 1: Comparison of fiducial markers and drift correction methods. (A) Comparison of photon emission from nano-gold rods (25 x 550 nm; green), fluorescent TetraSpeck beads (100 nm; blue), or fluorescent nano-diamonds (100 nm; red), over 4000 frames of image acquisition using 647 nm laser excitation. Thirty thousand localizations from a FND corrected for stage drift using (B) cross-correlation, CC, (C) fiducial correction, FC, or (D) averaged fiducial correction, AFC; 20 nm scale bar. (E–G) Histograms of the drift corrected localizations. (H) Ratio of observed precision over predicted precision (O/P) for the three correction methods. (I) Symmetry index for the three correction methods, calculated by measuring the SD of localizations in *X* and *Y* axes and dividing the higher SD over the lower SD. (H, I) Numbers of independent FNDs measured are indicated inside the bars, and error bars represent SD.

the precision actually achieved in the final SMLM image. We sought to test this assumption by comparing the localization precision (denoted by σ) calculated using the maximum likelihood estimation algorithm (Table 1; Ovesny *et al.*, 2014; Rieger and Stallinga, 2014) to the SD of multiple localizations from a single light-emitting source (i.e., FND). Because σ is derived from the distribution of photons in a single PSF, whereas SD measures the variance in the distribution of multiple PSF localizations, we will refer to σ as predicted precision and SD as observed precision. Continuing the analysis of localizations from a single light emitter, the observed precision of AFC-corrected FND localizations closely matched the average predicted precision, suggesting that all stage movement was corrected (Table 1). In fact, repeated experiments showed that the observed precision of FND localizations after AFC was higher than the average

	Cross-correlation	Spline correction	AFC
Average predicted σ (nm)[a]	4.0	4.0	4.0
Observed SD, *X*-axis (nm)	6.0	4.8	3.8
Observed SD, *Y*-axis (nm)	11.3	10.9	3.9

[a]Localization uncertainty, Δ*x*, was calculated using the following maximum likelihood estimation algorithm (Rieger and Stallinga, 2014), for a point spread function over the α x α pixel area, signal photon count *N*, the spot width σ, and the number of background photons per pixel *b*:

$$\Delta x\big|^2_{\mathrm{MLE}} = \frac{\sigma^2 + a^2/12}{N}\left(1 + 4\tau + \sqrt{\frac{2\tau}{1+4\tau}}\right)$$

with τ roughly equal to the ratio between the background intensity b/α^2 and the peak signal intensity $N/2\pi\sigma^2$:

$$\tau = \frac{2\pi b\left(\sigma^2 + a^2/12\right)}{Na^2}$$

The SD in the *X* and *Y* axes were measured for the distribution of localizations after correcting for stage drift using the method indicated in the top row.

TABLE 1: Comparison of drift correction methods.

predicted precision, as evidenced by the ratio of the observed to predicted localization precision (*O*/*P*; 0.71 ± 0.07, AFC; 146 FNDs; Figure 1H). In contrast, cross-correlation and fiducial correction yielded twofold-to-threefold lower observed precision than predicted as measured by the *O*/*P* ratio (3.23 ± 2.14, CC; 2.20 ± 2.07, FD; 26 FNDs; Figure 1H). These results show that FNDs are a superior SMLM fiducial marker, that AFC outperforms regression-based drift correction methods, and that proper drift correction is essential to achieve adequate precision in the final SMLM image.

Characterizing the localization distribution

Applying AFC to successive localizations from a single fluorescence source (i.e., FND) resulted in a radially symmetric distribution of localizations (Figure 1D). Because accurate identification of the light-emitter position is limited by this distribution, we sought to understand its origin. A previous study suggested that the distribution reflects stochastic numbers of photons captured over successive image frames, which lead to variability in localization precision (Sengupta *et al.*, 2011). To test whether the variation in prediction precision leads to the distribution of successive localizations, we compared the observed variance in localizations from an FND with predicted precision values ranging from 3.44 to 5.11 nm (Varied; 972 localizations; Supplemental Figure S2A; average σ = 4.04 ± 0.29 nm) to those binned between 3.99 and 4.01 nm after AFC (Restricted; 977 localizations; Supplemental Figure S2C; average σ = 4.00 ± 0.01 nm). We detected almost no difference in their observed precision (3.3, 3.5 nm Varied vs. 3.3, 3.4 nm Restricted [*X*, *Y*]; Supplemental Figure S2, B and D) or maximum distribution width (22.7 nm Varied vs. 24.3 nm Restricted; Supplemental Figure S2, B and D), suggesting that the variation in predicted precision does not significantly contribute to the observed localization distribution.

Alternatively, we asked whether the localization distribution reflects the inherent uncertainty in locating the single light-emitter position. Because σ measures SEM and implies random sampling from a normal distribution, we tested whether multiple localizations from a single light-emitting source follow such a distribution. Indeed, the distribution of AFC-corrected localizations from a single FND closely fit a Gaussian distribution, as 71.2% of the distribution fell within 1σ, 96.1% within 2σ, and 99.7% within 3σ (2000 localizations; Supplemental Figure S2, E and F). This normal fit was confirmed by the Anderson–Darling test ($h = 0$; $p = 0.13$, 0.08 [*X*, *Y*]; Supplemental Figure S2G). Therefore we tested whether the

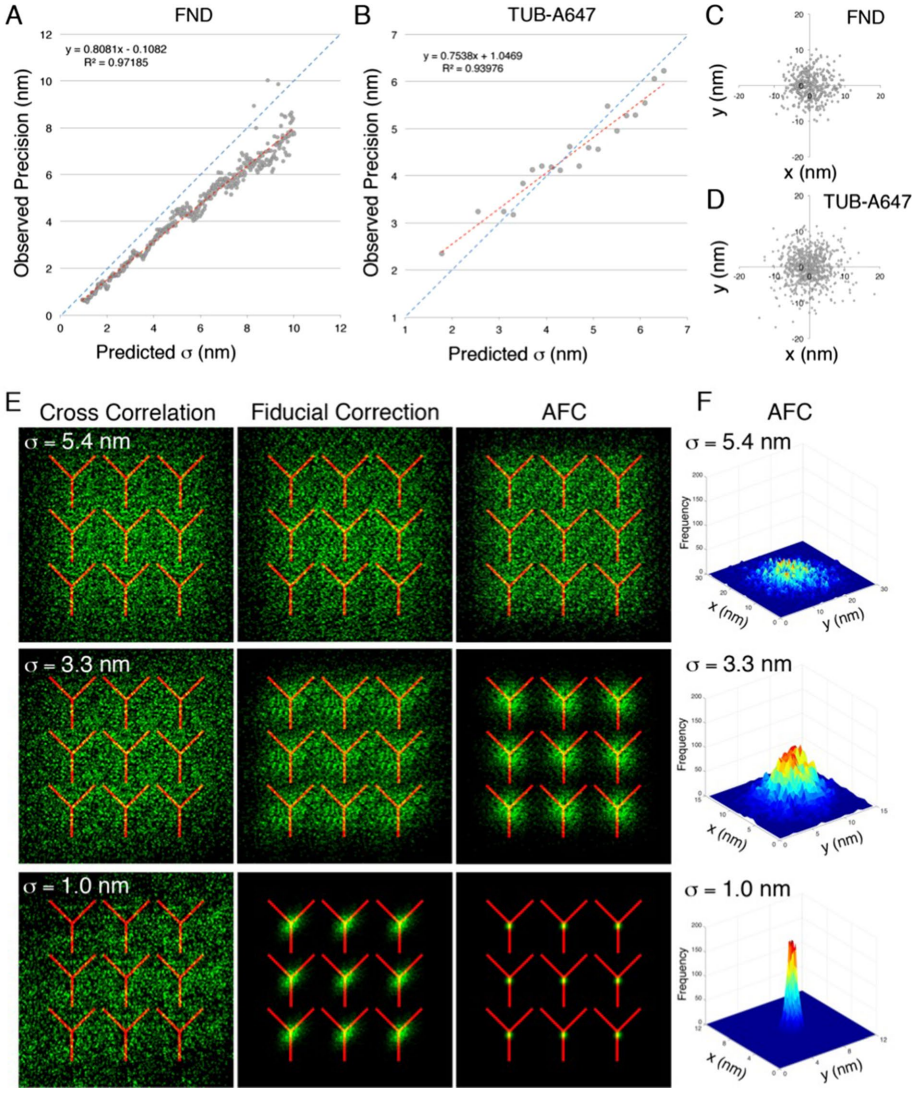

FIGURE 2: Modeling the localization distribution required for single-molecule accuracy. Observed precision for localizations (Y axis) plotted against the binned predicted σ (*X* axis) for FND (A) and TUB-A647 (B). Red dotted line is best-fit regression line for measured observed precision/predicted *s* and blue dotted line for observed precision/predicted σ = 1. *X-Y* scatter plot of localizations from a single FND (C) or localizations from TUB-647 antibody with σ = 4.5 nm average predicted precision (D). (E) Localizations from a FND overlaid with nine antibodies drawn to scale (12 nm width, 12 nm height) replicated in a 3 x 3 grid spaced 12 nm apart. (E) FND localizations at average predicted precision of σ = 5.4 nm (top row), σ = 3.3 nm (middle row), or σ = 1.0 nm (bottom row) were corrected for stage drift using cross-correlation (1st column), fiducial correction (2nd column), or averaged fiducial correction, AFC (3rd column). (F) Histogram of AFC-corrected localizations. (E, F) Average predicted precision indicated at the top left corner of each row.

distribution of localized peaks from multiple light-emitting sources correlates with their predicted precision across a range of precision values. To do this, we corrected FND localizations using AFC and binned them based on their respective predicted precisions. As shown in Figure 2A, the observed distribution of localizations (Observed Precision) correlated strongly with the binned predicted precision (Predicted σ; $R^2 = 0.97$; 95 FNDs).

Similar correlation was observed with Alexa 647–conjugated antibody-binding α-tubulin (Tub-A647; $R^2 = 0.94$, $n = 71$ antibody molecules; Figure 2B), although at lower observed precision than FNDs, possibly due to the presence of multiple dyes on each antibody molecule (2.4 dye/antibody). Localizations from Tub-A647 fit a normal distribution (Figure 2D). Of importance, the distribution size was similar for fluorophores with the same predicted precision whether they were FNDs (373 localizations; average σ = 4.5 ± 0.1 nm; SD = 3.8, 3.6 nm [*X*, *Y*], Figure 2C) or Tub-A647 (719 localizations; average σ = 4.5 ± 0.3 nm; SD = 4.4, 4.3 nm [*X*, *Y*], Figure 2D). Together these results indicate that each localized peak represents a sample of a distribution of localized peaks from the same light-emitting source and that the variance of the distribution correlates with the predicted precision.

Single-molecule accuracy

Quantitative analysis of cellular protein assemblies at the single-molecule level is a major goal of SMLM. Regarding the goal of SMLM in detecting single-molecule positions, past studies were restricted to global estimates of the targeted population (Sengupta *et al.*, 2013; Sherman *et al.*, 2013) or relatively large structures with known molecular patterns (Szymborska *et al.*, 2013; Sochacki *et al.*, 2014). Without a proper framework for single-molecule imaging and analysis, SMLM has largely been used as a superior structural imaging technique rather than as a tool for investigating the nanoscale architecture and single-protein topology of molecular networks.

To facilitate the latter aim of SMLM, we examined the conditions required for accurate localization of single molecules. Because accurate identification of a single light-emitter position is limited by the distribution of its localized peaks and the variance of this distribution becomes smaller with higher precision (Figure 2, A and B), we sought to find the minimum predicted precision at which the distribution size becomes smaller than the size of an antibody (~12 nm), thus allowing robust discrimination of single-molecule positions using dSTORM (i.e., single-molecule accuracy). To do this, we localized FNDs emitting different numbers of photons and corrected them using the three methods of drift correction. Each distribution of FND localizations was then replicated in a 3 × 3 grid with the centers of the distributions spaced 12 nm apart (the dimension of an antibody molecule) to model a densely labeled sample and overlaid with nine antibodies drawn to scale (12 × 12 nm).

At an average predicted precision of σ = 5.4 nm, none of the correction methods allowed discrimination of antibody positions, as the area covered by the localization distribution was larger than the antibody size and overlapped with neighboring distributions (Figure 2, E and F, top). At σ = 3.3 nm, only the AFC-corrected FND localizations resulted in nonoverlapping determination of antibody locations, with >95.5% (2σ) of localizations distributed within the 12-nm antibody size (SD = 2.5, 2.5 nm [*X*, *Y*], AFC, Figure 2, E and F, middle). At σ = 1.0 nm, both fiducial and AFC-corrected localizations showed discrete visualization of antibody locations (Figure 2E,

bottom). Moreover, we measured subnanometer-level precision in the distribution of AFC-corrected localizations (SD = 0.5, 0.5 nm [*X*, *Y*]; Figure 2, E and F, bottom), matching the level of precision achieved with feedback loop–based stage drift elimination (Pertsinidis *et al.*, 2010). These results show that drift correction with cross-correlation is not capable of achieving single-molecule accuracy, whereas fiducial correction does so only at an extremely high precision level. Therefore, to achieve single-molecule accuracy with 95.5% confidence (2σ), we chose FNDs as the fiducial marker, AFC as the drift correction method, and σ = 3 nm as the minimum threshold level of precision for inclusion in SMLM analysis.

Next we sought to optimize dSTORM imaging conditions to achieve single-molecule accuracy in a cell sample labeled with A647-conjugated antibody. Increasing the camera exposure time from 10 ms (typically used in dSTORM studies) to 200 ms allowed approximately three times more photons to be captured from A647 dyes (1908 average photons/localization, 10-ms exposure; 5871 average photons/localization, 200-ms exposure). Use of a 1.5× intermediate-magnification lens increased observed precision by 0.5 nm (Supplemental Figure S3A). Also, in contrast to the blocking buffers frequently used in dSTORM, 1% fish-scale gelatin showed no detectable autofluorescence when excited with a high-intensity 647-nm laser, reducing background noise (Supplemental Figure S3B). Finally, we tested different photoswitching solutions and found that a combination of 100 mM 2-mercaptoethanol, 20 mM 2-mercaptoethylamine, and 2 mM cyclooctatetraene (Olivier *et al.*, 2013) allowed the highest A647 signal intensity, resulting in a predicted precision of 2.4 nm (mode) for an activated Jurkat T-cell labeled with A647-conjugated antibody against phosphorylated SLP-76 (pSLP76-A647; Supplemental Figure S3C), providing numerous localizations that meet the threshold criterion for single-molecule accuracy.

madSTORM

Whereas a number of multiprotein structures have been elegantly studied using SMLM (Betzig *et al.*, 2006; Bates *et al.*, 2007; Szymborska *et al.*, 2013; Sochacki *et al.*, 2014), small heterogeneous complexes such as the TCR microcluster have not been well characterized due to limits in both localization accuracy and multiplexing. To overcome these issues, we developed a technique called multiplexed antibody size-limited dSTORM (madSTORM), which allows targeting of multiple epitopes using sequential binding and elution of antibodies (Supplemental Figure S4).

We tested different buffers for their ability to elute antibody from the cell sample. Because integrity of the cell sample is paramount to accommodate several rounds of madSTORM imaging, we sought to use buffers with moderate pH (4–8) at room temperature. For Jurkat T-cells fixed and stained with A647-conjugated antibody-binding phosphorylated TCRζ (pTCRζ-A647) a solution containing 3.5 M $MgCl_2$, 20 mM 1,4-piperazinediethanesulfonic acid (PIPES), and 0.1% Tween-20 (pH 6.5) proved to be most effective (Figure 3A), removing >90% of pTCRζ-A647 as measured by the decrease in fluorescence over five washes with the solution (Figure 3B). This buffer was also effective at eluting other A647-conjugated antibodies (Supplemental Figure S5), suggesting its use as a universal elution buffer.

Furthermore, by comparing the loss in fluorescence in cells either bound or bound and cross-linked to pTCRζ-A647 using 4% paraformaldehyde, we showed that most of the fluorescence loss with elution buffer occurs due to release of antibody from epitopes (Supplemental Figure S6). In addition, signals from ZAP70–yellow fluorescent protein (YFP) and A647-conjugated antibody binding ZAP70 (ZAP70-A647) after multiple washes with the elution buffer showed that microcluster structures remained intact (Supplemental Figure S7), suggesting that the cell sample remained cross-linked after exposure to elution buffer.

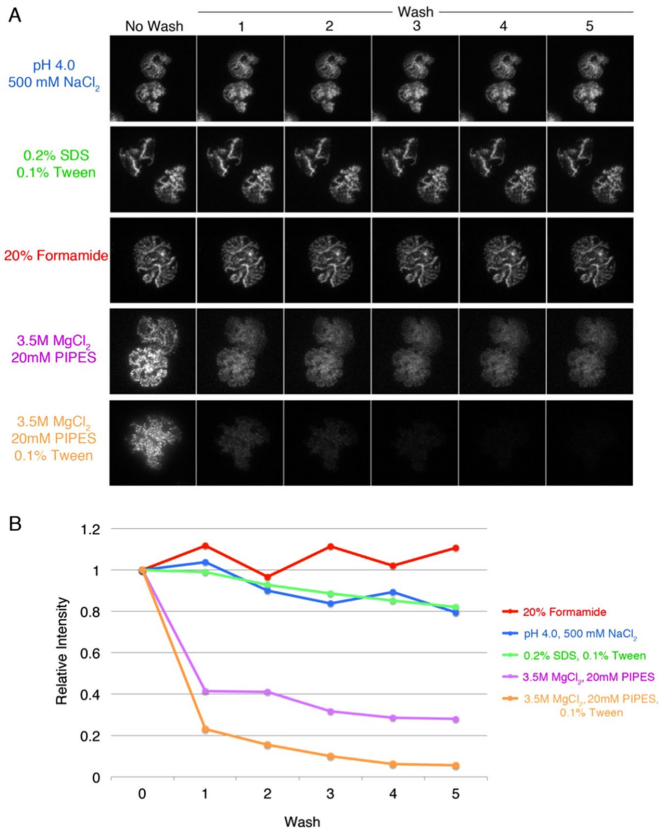

FIGURE 3: The effect of buffers on elution of antibody from cell sample. Release of antibody from the cell sample assayed by fluorescence decrease after the indicated number of washes with elution buffer. (A) TIRF images of activated Jurkat T-cells labeled with pTCRζ-A647 and washed with buffers indicated on the left. (B) Plot of pTCRζ-A647 signal intensities shown in A normalized against the signal in the "No Wash" image.

To test the effect of the elution buffer on individual molecule positions, we performed madSTORM imaging using A647-conjugated antibody-binding phosphorylated LAT (pLAT-A647 [Y171]) and analyzed the molecular localizations after three rounds of multiplexing using the same antibody. The shift in single LAT-molecule positions (average 9.88 ± 3.68 nm, eight molecules) was comparable to the expected offset measured by the changes in individual FND positions over successive multiplexing rounds (average 7.55 ± 1.86 nm, three FNDs; Supplemental Figure S8A). Further, we did not observe a change in the overall distribution of LAT proteins between the three rounds of multiplexing as measured by the O-ring bivariate analysis (average 96.6 ± 3.9% confidence level of homogeneous mixing; Supplemental Figure S8B; Wiegand and Moloney, 2004; Sherman *et al.*, 2013), showing that molecular positions are not altered by repeated exposure to elution buffer during madSTORM imaging.

Whereas photobleaching of Alexa 647 is an irreversible process involving photooxidative cleavage of the dye molecule, as shown for the closely related cyanine dyes (Stennett *et al.*, 2014), it can alternatively be photoswitched into reversible dark states. To detect the photoswitched fraction of Alexa 647 (which could reactivate and contaminate subsequent signals), we performed either photobleaching

alone or elution and photobleaching of pTCRζ-A647 and measured the total fluorescence signal after 1 h of incubation in phosphate-buffered saline (PBS), mimicking the time line of multiplexing during madSTORM. We measured negligible fluorescence signal after combined elution and photobleaching of pTCRζ-A647 (0.23% of original signal), which was ~10-fold lower than photobleaching alone (2.69% of original fluorescence signal), showing that the elution step in madSTORM greatly negates cross-talk during serial multiplexing (Supplemental Figure S9).

madSTORM imaging of activated T-cells

Multicolor dSTORM imaging of activated T-cells has been limited to two colors due to limited availability of high-performing fluorescent dyes (Dempsey *et al.*, 2011; Soares *et al.*, 2013) and lacked precise spatial alignment between channels due to nonlinear chromatic aberration (Erdelyi *et al.*, 2013). To overcome these issues, we performed madSTORM imaging of activated T-cells. Jurkat cells were activated on an anti-CD3ε antibody–coated coverslip, and seven different proteins were imaged in a single cell using A647-conjugated probes (Figure 4A and Supplemental Figure S10A) with <0.01% cross-talk among images (Supplemental Figure S10, B and C). FND fiducial markers were also used for spatial alignment of sequentially multiplexed localization data, achieving an average alignment error between madSTORM images of 3.6 ± 2.7 nm (Composite, Figure 4A) as measured by the offset in the global center position of designated FNDs across multiplexed images (visible in Elution + Photobleaching, Supplemental Figure S10A).

Despite the successful visualization of multiple targets, there were several issues to consider when using madSTORM. Because certain structures were located beyond the optimal plane of total internal reflection fluorescence (TIRF) illumination (e.g., endoplasmic reticulum, vimentin), their localizations did not meet the 3-nm precision threshold (marked by an asterisk in Figure 4A), indicating that single-molecule accuracy may not be attainable for some cytosolic targets. In addition, we observed very poor A647–phalloidin (Ph-A647) signal in cells washed once with elution buffer (Figure 4B and Supplemental Figure S11). This was not due to physical loss of F-actin filaments, as the green fluorescent protein (GFP)–actin signal was not affected by the elution buffer (Figure 4B and Supplemental Figure S11), suggesting that elution buffer alters the quaternary conformation of F-actin required for phalloidin binding, similar to the effect of methanol fixation (Burkel *et al.*, 2007). Thus we opted to image with Ph-A647 before washing with the elution buffer (Supplemental Figure S11A). Moreover, this effect was used to our advantage, as washes with elution buffer proved to be far more efficient at removing the Ph-A647 signal than photobleaching alone (unpublished data).

SMLM techniques usually require a trade-off between resolution (requires high signal density) and localization accuracy (requires high precision), as strategies used to boost signal density (use of secondary antibody, shorter exposure time, inclusion of less precise localizations, etc.) concomitantly reduce the accuracy of localized signals. Conversely, in the case of madSTORM, signal density has been sacrificed to attain high localization accuracy by using directly labeled primary antibody, a longer exposure time (200 ms), and a rigorous precision threshold (3 nm). The consequence of choosing localization accuracy over resolution is apparent in the following SMLM images of clathrin-coated pits using A647-conjugated antibody–binding clathrin heavy chain (Clathrin HC-A647). At single-molecule accuracy, the location of individual Clathrin HC-A647 molecules was visible but not the ringed shape of clathrin-coated pits (Figure 4C). In contrast, the ringed shapes of clathrin-coated pits were seen in images acquired with a shorter exposure time (20 ms)

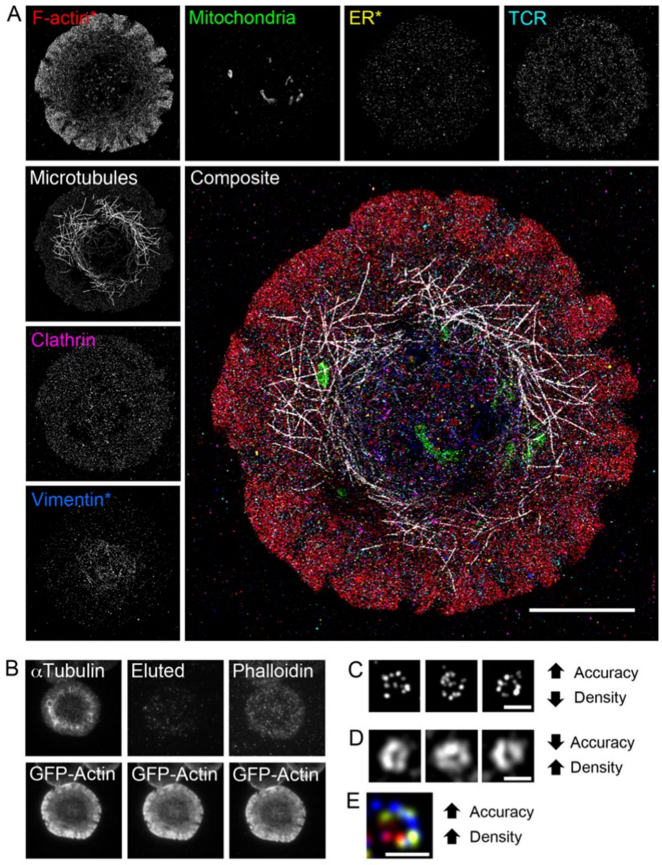

FIGURE 4: Multiplexed imaging of cellular structures using madSTORM. (A) Cellular structures in an activated Jurkat T-cell sequentially labeled by the following A647-conjugated probes: F-actin, Ph-A647; microtubules, Tub-A647; clathrin, Clathrin HC-A647; mitochondria, HSP60-A647; TCR, pTCRζ -A647; ER, Calnexin-A647; vimentin, Vimentin-A647 (top row, left column), and composite image of all madSTORM images (bottom right); 5 μm scale bar. Asterisk marks madSTORM images lacking single-molecule accuracy. Colors in the composite image correspond to the indicated colored label in the top row and left column of panels. (B) Jurkat cell stably expressing GFP-actin, fixed and stained with Tub-A647, washed once with elution buffer, and stained with Ph-A647. Clathrin-coated pits labeled by Clathrin HC-A647 imaged with (C) high localization precision (<3 nm) and low signaling density or (D) low localization precision (<20 nm) and high signaling density. (E) Clathrin-coated pit labeled with Clathrin HC-A647 over 1 (red), 2 (green), and 3 (blue) sequential rounds of multiplexing. (C–E) Scale bars, 100 nm.

and less rigorous precision threshold (20 nm) but not individual Clathrin HC-A647 locations (Figure 4D). However, resolution and accuracy are not mutually exclusive, as the madSTORM technique could be used repeatedly using the same antibody, allowing both high labeling density and high localization precision. This is evident in the composite image of a clathrin-coated pit after three rounds of madSTORM imaging using Clathrin HC-A647 (Figure 4E).

Finally, we sought to target the individual molecular components of the TCR microcluster and expand the number of multiplexed epitopes visualized using madSTORM. We localized 25 different epitopes with 2.6 ± 0.1 nm average localization precision (202,449 localizations), 2.0 ± 1.7 nm average alignment error, and <0.01% net cross-talk (Supplemental Figure S12). The resulting composite madSTORM image of six of the TCR signaling components showed discrete visualization of the molecular constituents of individual TCR microclusters

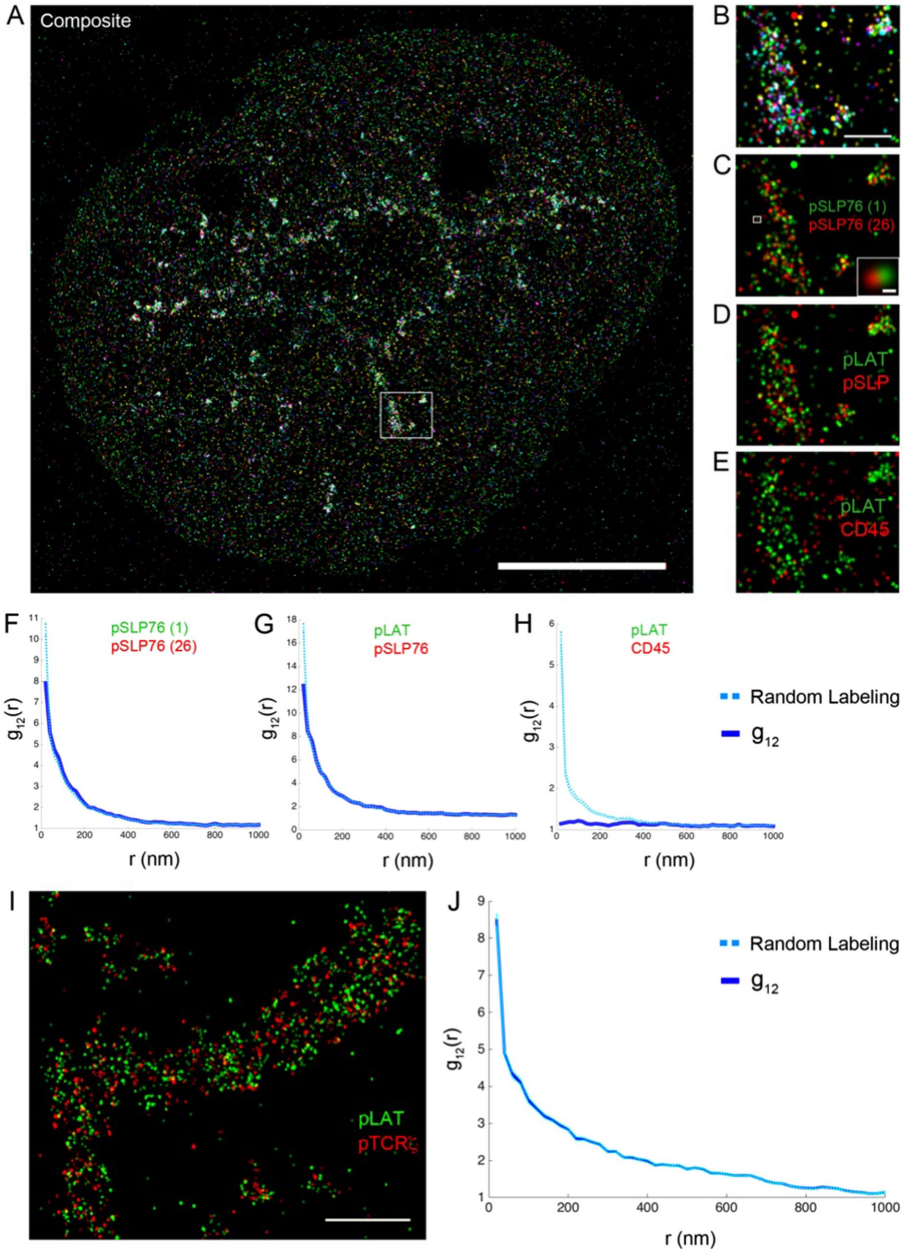

FIGURE 5: TCR microcluster components visualized using madSTORM. (A) Composite of the following antibodies imaged using madSTORM: pLAT-A647 (Y171), green; pSLP-A647, red; pTCRζ-A647, blue; pLAT-A647 (Y191), cyan; pSRC-A647, magenta; pPLCγ1, yellow; 5 μm scale bar. (B) Zoomed image of the boxed region in A; 100 nm scale bar. (C) Zoomed composite image of the boxed region in A showing pSLP76-A647 localized at the 1st (green) and 26th (red) round of multiplexing. Bottom right inset is a zoomed image of the boxed region in C and shows adjacent localization of a single pSLP76-A647 molecule at different multiplexing rounds; 20 nm scale bar. (D) Zoomed composite image of pLAT-A647 (Y171) (green) and pSLP76-A647 (red) or (E) CD45-A647 (red). (F–H) Plot of Wiegand-Moloney o-ring bivariate analysis with antibody pairs indicated at the top. Random labeling of molecule populations is indicated by the light blue dotted line, and the measured bivariate correlation is indicated by the dark blue solid line. (I) Zoomed composite image of pLAT-A647 (Y171) (green) and pTCRζ-A647 (red) and (J) corresponding plot of Wiegand-Moloney o-ring bivariate analysis; 0.5 μm scale bar in I.

at single-molecule accuracy (Figure 5, A and B). Moreover, comparison of SLP76-A647 signals at imaging rounds 1 and 26 showed the same pattern of staining (Supplemental Figure S12), coincident localization of single molecules (Figure 5C, bottom right inset), and high mixing level calculated from Wiegand–Moloney bivariate analysis (86% confidence level of homogeneous mixing, Figure 5F; Wiegand and Moloney, 2004; Sherman *et al.*, 2013). Bivariate analysis of multiplexed localization data confirmed the expected interactions between phosphorylated LAT (Y171) and other TCR signaling molecules such as SLP76 (Figure 5, D and G) and exclusion of phosphorylated LAT from positions of the phosphatase CD45 (Figure 5, E and H; Bunnell *et al.*, 2002).

Previous PALM studies reported conflicting results regarding the localization of TCR and LAT molecules at the immunological synapse. In particular, TCRζ and LAT clusters were observed as distinct ~100-nm-sized "protein islands" (Lillemeier *et al.*, 2010) or as partially overlapping nanodomains (Sherman *et al.*, 2011). In contrast, we observed almost homogeneous mixing of phosphorylated LAT and TCRζ molecules in activated Jurkat cells analyzed at single-molecule accuracy (94.2 ± 12.0% confidence level of homogeneous mixing, four cells; Figure 5, I and J). The discrepancy in the TCR and LAT localizations may be due to the targeting of phosphorylated populations, high-precision thresholding (3 nm), or the sequential targeting of cell samples used in our study. Multivariate analysis of microcluster components will be performed in future madSTORM experiments to confirm and extend these observations.

DISCUSSION

madSTORM provides a framework for both large-scale multiplexing and single-molecule accuracy, enabled by the use of FNDs as fiducial markers for drift correction and alignment. As such, madSTORM can be viewed as a topology tool, mapping the locations of diverse molecules within structures and complex signaling networks at single-molecule accuracy. This is in contrast to the common application of SMLM in imaging the shapes and patterns of structures, which requires significantly higher signal density of probes than is possible using antibody-based SMLM methods (Kiuchi *et al.*, 2015; Legant *et al.*, 2016). For these reasons, signal density has been sacrificed to achieve the high localization precision needed for single-molecule accuracy. However, our multiplexing technique can achieve higher signal density either by shortening the exposure time and setting a less rigorous threshold for localization precision or by multiplexing with the same antibody repeatedly.

The protocol described in this study provides a founding template for large-scale, serial multiplexing using a combination of photobleaching and antibody elution. However, because we observed a variability in the efficiency of antibody removal (50–95%; Supplemental Figure S13), we expect that the composition of the elution buffer will be adjusted for each antibody to provide an optimal combination

of antibody removal and cell sample preservation in future studies. Moreover, the order of multiplexing should be arranged based on the sensitivity of the antibodies to the elution buffer, starting from the best-eluting antibody, to maximize multiplexing capacity. Note that use of the elution buffer without Tween-20 (removes ~80% of bound antibody) may be required for sensitive membrane structures to avoid possible disruption of hydrophobic interactions in the membrane.

For this study, FNDs were bound to the PLL-coated glass coverslip and imaged in two dimensions using TIRF microscopy. Adapting our technique to three dimensions will require labeling the cell surface with functionalized FNDs at various *z*-positions or embedding a solid material with a high density of FNDs to serve as a 3D registration matrix, as well as expansion of the AFC algorithm for use in 3D superresolution images (e.g., iPALM, 3D-STORM).

We showed that the extent of the localization distribution determines the level of accuracy of single-molecule positions. However, because "single-molecule" refers to the fluorophore and not the targeted epitope, the size of the probe must be considered in relative measurements such as molecule distance or stoichiometry. In addition, because each antibody is conjugated to multiple fluorescent dyes at dispersed sites, distinct localizations may be observed for each antibody molecule. To avoid this potential complication, conjugation of dyes at specific sites on the antibody will be considered in future experiments.

SMLM studies have relied on various "grouping" algorithms to deal with multiple localizations from a single fluorophore. These algorithms attribute successive localizations from a defined region to a single molecule but cannot determine whether nonsuccessive localizations are from the same molecule or neighboring molecules. In contrast, we showed that limiting localization distribution to the antibody size allows robust discrimination of localizations from single molecules. This antibody-size-limited accuracy should allow grouping of single light-emitting molecules regardless of their order of localization.

We performed 26 rounds of multiplexing with identical localization of the same epitope from the first and last round of madSTORM imaging. For future experiments, the order of multiplexing will be reversed or randomly scrambled to test the efficiency of binding for all localized epitopes during large-scale multiplexing. Furthermore, because a limited percentage of epitopes is likely bound by antibody during a single round of madSTORM imaging, each epitope will be targeted repeatedly to ensure localization of the full population of epitopes. This will enable quantitative analysis of madSTORM data such as molecular counting and possibly yield new insights into the complex network of heterogeneous signaling systems. Moreover, new analytical methods are required to process the highly multiplexed single-molecule data acquired using madSTORM in future studies.

MATERIALS AND METHODS

Antibodies and reagents

Murine monoclonal antibodies used to activated T-cells in coverslip binding assays were obtained from BD Biosciences (San Jose, CA; anti-CD3ε, UCHT1). A647-conjugated phalloidin was purchased from Molecular Probes (Eugene, OR; A22287). Primary antibodies were purchased as follows: mouse monoclonal anti–α-tubulin antibody from Sigma-Aldrich (St. Louis, MO; T6199), mouse monoclonal anti–clathrin heavy chain antibody from Thermo (Waltham, MA; MA1-065), A647-conjugated mouse monoclonal anti-HSP60 antibody from BD Biosciences (558684), mouse monoclonal anti-TCRζ (pY142) antibody from BD Biosciences (558402), A647-conjugated mouse monoclonal anti-calnexin antibody from Abcam (Cambridge, MA; ab202572), A647-conjugated rabbit monoclonal anti-vimentin antibody from Cell Signaling (Danvers, MA; 9856S), mouse monoclonal anti-SLP76 (pY128) antibody from BD Biosciences (558367), mouse monoclonal anti-LAT (pY171) antibody from BD Biosciences (558392), rabbit polyclonal anti-LAT (pY191) antibody from Cell Signaling (3584BF), mouse monoclonal anti–c-Cbl antibody from BD Biosciences (610442), mouse monoclonal anti-ITK antibody from Cell Signaling (2380BF), A647-conjugated rabbit monoclonal anti–COX IV antibody from Cell Signaling (7561S), mouse monoclonal anti-CD45 antibody from BD Biosciences (555480), A647-conjugated mouse monoclonal anti-AKT antibody from Cell Signaling (2944S), A647-conjugated mouse monoclonal anti-p44/42 mitogen-activated protein kinase (Erk1/2; pY204) antibody from Cell Signaling (4375S), mouse monoclonal anti-LAT (pY226) antibody from BD Biosciences (558432), rabbit monoclonal anti-ZAP70 (pY319) antibody from Cell Signaling (2717BF), rabbit monoclonal anti-PLCγ1 (pY783) antibody from Cell Signaling (14008BF), rabbit polyclonal anti-Src (pY418) antibody from Sigma-Aldrich (SAB4504536), A647-conjugated mouse monoclonal anti–β-catenin (pY319) antibody from Cell Signaling (4627S), mouse monoclonal anti-TOM20 antibody from BD Biosciences (612278), mouse monoclonal anti-Grb2 antibody from BD Biosciences (610112), and A647-conjugated mouse monoclonal anti–Nucear Pore O-Linked Glycoprotein (NPoG) antibody from Novus Biologicals (Littleton, CO; NB600-1068AF647). Mouse monoclonal anti-paxillin antibody (BD Biosciences; 610052) was a gift from the C. Waterman-Storer lab.

Cell culture and stable cell lines

E6.1 Jurkat cells were cultured in RPMI (11875-093; Life Technologies, Carlsbad, CA), 10% fetal bovine serum (26140-079; Life Technologies), and 1% penicillin–streptomycin (15070-063; Life Technologies). Generation of E6.1 Jurkat cell lines stably expressing ZAP70-YFP and GFP-actin has been described previously (Bunnell *et al.*, 2002). $CD4^+$ mouse T-cells from lymph node single-cell suspensions were isolated using a Dynal mouse CD4-negative isolation kit (Miltenyi Biotec) according to the manufacturer's instructions and as described previously (Rouquette-Jazdanian *et al.*, 2015). Cells were >85% $CD4^+$ after purification. Purified $CD4^+$ LN cells were then resuspended in prewarmed RPMI 1640 at 1×10^6 cells/10 µl.

Imaging and data collection

TIRF images were acquired using a Nikon Eclipse Ti inverted microscope, a 647-nm acousto-optic tunable filter–modulated LUNB solid-state laser (125 mW), a 100× SR Apochromat TIRF objective lens (1.49 numerical aperture), and an Andor iXon Ultra 897 EM charge-coupled device camera (512 × 512 pixels, 16 µm pixel). A 1.5× intermediate-magnification lens was used for madSTORM. madSTORM localization of TIRF confocal images was performed using ThunderSTORM plug-in (version 1.2; Ovesny *et al.*, 2014) on Fiji software at a pixel size of 100 nm, photoelectrons per A/D count of 4.28, base level A/D count of 100, EM gain of 100, PSF integrated Gaussian localization, 5-pixel fitting radius, maximum likelihood fitting method, and 1.3-pixel initial sigma. Averaged fiducial correction of madSTORM localization data and alignment of multiple localization data were performed using custom codes written in MATLAB (R2014b). madSTORM images were rendered after merging molecule localizations at 12 nm using ThunderSTORM with a normalized Gaussian method with lateral uncertainty of 12 nm for visualization of the entire cell sample and 3-nm lateral uncertainty for zoomed images of selected regions. Localizations with uncertainty >3 nm were filtered out of the final localization data set. The final localization data set was merged at a maximum distance of 12 nm, 0 max frames per molecule, and 20,000 frames (or total

image frames) for max off frames using ThunderSTORM software to remove multiple detections of the same fluorophore. Bivariate analysis of the final, merged localizations and calculation of their mixing levels were performed as previously described (Sherman *et al.*, 2011). Calculation of cross-talk in madSTORM images was performed by dividing the integrated signal intensity from the same region of "elution + photobleach" sum stack image from the "TIRF" sum stack image after normalizing for EM gain.

madSTORM imaging and elution buffers

The madSTORM imaging buffer was prepared following method B from the Nikon N-STORM protocol, except that we added 100 mM 2-mercaptoethanol (M7154; Sigma-Aldrich), 20 mM cysteamine (30070; Sigma-Aldrich), and 2 mM cyclooctatetraene (138924; Sigma-Aldrich). The elution buffer consisted of 3.5 M $MgCl_2$ (M9272; Sigma-Aldrich) adjusted to pH 6.0, 20 mM PIPES (P6757; Sigma-Aldrich), and 0.1% Tween-2 (BP337-500; Fisher Scientific, Hampton, NH). The elution buffer was warmed in a 37°C water bath for 15 min and vortexed for 1 min to ensure solubility.

Drift correction algorithms

We used the cross-correlation and fiducial correction algorithms included in the ThunderSTORM software (Ovesny *et al.*, 2014). The observed precision SD was measured from FNDs used in the algorithm for cross-correlation, in contrast to a separate set of FNDs for fiducial correction and averaged fiducial correction. The settings used for cross-correlation and fiducial correction in ThunderSTORM were optimized for each image, but typically we used 100 localizations/bin for cross-correlation and 0.01 trajectory smoothing factor for fiducial correction. For fiducial and averaged fiducial correction methods, FNDs in the TIRF image (detected as spots of constant emission) were isolated and localized individually using ThunderSTORM. Averaged fiducial correction for an arbitrary set of localization microscopy images consisting of *t* frames containing localizations of *N* fiducial FNDs and *M* localizations from each frame of the experimental sample (EXP) were performed in the following steps. Note that FNDs must be present in all frames, whereas EXP does not. EXP can also be a second set of nanodiamonds.

Step 1: Generating the averaged FND position in each frame (avgX_j, avgY_j). In every frame, the positions of all FNDs (*X*, *Y*) were averaged, producing a single set of coordinates (avgX, avgY) that gave a single average location for all the FNDs in that frame.

For frame *j*,

$$\text{avg}(X)j = \left(\sum_{n=1}^{N}(X(\text{FND}n)j\right) / (N)$$

$$\text{avg}(Y)j = \left(\sum_{n=1}^{N}(Y(\text{FND}n)j\right) / (N)$$

where *n* is the FND number ($n = 1, N$) and *j* is the frame number ($j = 0, t$).

This generated a set of size t containing the values of the coordinates for the average location of all FNDs in each frame.

Step 2: Calculating the displacement in averaged FND positions (avgΔX_j, avgΔY_j). The averaged FND position for each frame was subtracted from the averaged FND position in frame 1 to yield the displacement in averaged FND position, (avgΔX, avgΔY).

For frame *j* and FND*n*,

$$\text{avg}\Delta X_i = \text{avg}X_1 - \text{avg}X_j$$

$$\text{avg}\Delta Y_j = \text{avg}Y_1 - \text{avg}Y_j$$

where *j* is the frame number ($j = 0, t$).

This produced a set containing the values of the coordinates for the final, corrected locations of all FNDs for every frame.

Step 3: Generating the AFC-corrected positions of all experimental localizations (new X(EXPm)$_j$, new Y(EXPm)$_j$). For the same set of images, the positions of all the experimental localizations were corrected by subtracting the displacement in averaged FND positions from the coordinates of each localization in every frame, generating a new position corrected with respect to the multiple FNDs.

For frame j and EXP*m*,

$$\text{new } X(\text{EXP}m)_j = X(\text{EXP}m)_j - avg\Delta X_j$$

$$\text{new } Y(EXPm)_j = Y(\text{EXP}m)_j - \text{avg}\Delta Y_j$$

where *m* is the localization number ($m = 1, M$) and *j* is the frame number ($j = 0, t$).

Code availability. The custom Matlab code used to perform the foregoing averaged fiducial correction will be made available to download online.

madSTORM protocol

A647 dye was conjugated to antibodies using the antibody labeling kit from Molecular Probes (A20186). Eight-well coverslip chambers (155409; Lab-Tek) were prepared for the cell spreading assay as described previously (Bunnell *et al.*, 2003), except that 100-nm nitrogen-vacancy fluorescent nanodiamonds were vortexed for 5 min, sonicated for 30 s, and added to the PLL-coated coverslip chambers for 15 min before being coated with anti-CD3ε antibodies. Jurkat T-cells or $CD4^+$ mouse T-cells were stimulated for 3 min on the anti-CD3ε–coated coverslip chambers in 4-(2-hydroxyethyl)-1-piperazineethanesulfonic acid–buffered saline with 1% fetal bovine albumin (98-100P; KSE Scientific) as described previously (Campi *et al.*, 2005). Activated cells were fixed for 30 min with 2.5% paraformaldehyde (18501; Ted Pella), permeabilized for 5 min with 0.1% Triton-X (T9284; Sigma-Aldrich), blocked for 30 min with 1% fish-scale gelatin (G7041; Sigma-Aldrich), and labeled with 50–100 nM A647-conjugated probes for 1 h at room temperature. The imaging field of view was selected based on inclusion of a well-labeled cell sample and at least four bright FNDs. Note that averaged fiducial correction performance improves with a higher number of FNDs. At least four FNDs were used as fiducial markers for both the averaged fiducial correction and alignment algorithms, and the other FNDs were used to measure the achieved precision and alignment. The cell sample was imaged for 20,000–30,000 frames in madSTORM imaging buffer, washed (three times) with 1× Tris-buffered saline (TBS; RGF-3385; KD Medical), washed for 1 min (three times) with elution buffer, washed (three times) with 1× TBS, photobleached for ~2 s in 1× PBS (KD Medical, RGF-3210), fixed for 10 min in 4% paraformaldehyde, and labeled with the next A647-conjugated probe for 1 h. Note that it is extremely important to keep the eight-well coverslip chamber in the same position on the microscope stage using metal clamps provided by Nikon throughout the madSTORM imaging procedure.

ACKNOWLEDGMENTS

We thank Connie Sommers for providing $CD4^+$ mouse T-cells, Sunmee Huh for help with illustration, Xufeng Wu for access to the Nikon N-STORM microscope, and Hari Shroff for comments on the manuscript. This research was supported by the Intramural Research Program of the National Cancer Institute Center for Cancer Research.

REFERENCES

Bates M, Huang B, Dempsey GT, Zhuang X (2007). Multicolor super-resolution imaging with photo-switchable fluorescent probes. Science 317, 1749–1753.

Bates M, Jones SA, Zhuang X (2013). Stochastic optical reconstruction microscopy (STORM): a method for superresolution fluorescence imaging. Cold Spring Harb Protoc 2013, 498–520.

Betzig E, Patterson GH, Sougrat R, Lindwasser OW, Olenych S, Bonifacino JS, Davidson MW, Lippincott-Schwartz J, Hess HF (2006). Imaging intracellular fluorescent proteins at nanometer resolution. Science 313, 1642–1645.

Bumb A, Sarkar SK, Billington N, Brechbiel MW, Neuman KC (2013). Silica encapsulation of fluorescent nanodiamonds for colloidal stability and facile surface functionalization. J Am Chem Soc 135, 7815–7818.

Bunnell SC, Barr VA, Fuller CL, Samelson LE (2003). High-resolution multicolor imaging of dynamic signaling complexes in T cells stimulated by planar substrates. Sci STKE 2003, PL8.

Bunnell SC, Hong DI, Kardon JR, Yamazaki T, McGlade CJ, Barr VA, Samelson LE (2002). T cell receptor ligation induces the formation of dynamically regulated signaling assemblies. J Cell Biol 158, 1263–1275.

Burkel BM, von Dassow G, Bement WM (2007). Versatile fluorescent probes for actin filaments based on the actin-binding domain of utrophin. Cell Motil Cytoskeleton 64, 822–832.

Campi G, Varma R, Dustin ML (2005). Actin and agonist MHC-peptide complex-dependent T cell receptor microclusters as scaffolds for signaling. J Exp Med 202, 1031–1036.

Dempsey GT, Vaughan JC, Chen KH, Bates M, Zhuang X (2011). Evaluation of fluorophores for optimal performance in localization-based super-resolution imaging. Nat Methods 8, 1027–1036.

Erdelyi M, Rees E, Metcalf D, Schierle GS, Dudas L, Sinko J, Knight AE, Kaminski CF (2013). Correcting chromatic offset in multicolor super-resolution localization microscopy. Opt Express 21, 10978–10988.

Gerdes MJ, Sevinsky CJ, Sood A, Adak S, Bello MO, Bordwell A, Can A, Corwin A, Dinn S, Filkins RJ, *et al*. (2013). Highly multiplexed single-cell analysis of formalin-fixed, paraffin-embedded cancer tissue. Proc Natl Acad Sci USA 110, 11982–11987.

Hess ST, Girirajan TP, Mason MD (2006). Ultra-high resolution imaging by fluorescence photoactivation localization microscopy. Biophys J 91, 4258–4272.

Hoebe RA, Van Oven CH, Gadella TW Jr, Dhonukshe PB, Van Noorden CJ, Manders EM (2007). Controlled light-exposure microscopy reduces photobleaching and phototoxicity in fluorescence live-cell imaging. Nat Biotechnol 25, 249–253.

Jungmann R, Avendano MS, Woehrstein JB, Dai M, Shih WM, Yin P (2014). Multiplexed 3D cellular super-resolution imaging with DNA-PAINT and Exchange-PAINT. Nat Methods 11, 313–318.

Kaizuka Y, Douglass AD, Varma R, Dustin ML, Vale RD (2007). Mechanisms for segregating T cell receptor and adhesion molecules during immunological synapse formation in Jurkat T cells. Proc Natl Acad Sci USA 104, 20296–20301.

Kiuchi T, Higuchi M, Takamura A, Maruoka M, Watanabe N (2015). Multitarget super-resolution microscopy with high-density labeling by exchangeable probes. Nat Methods 12, 743–746.

Legant WR, Shao L, Grimm JB, Brown TA, Milkie DE, Avants BB, Lavis LD, Betzig E (2016). High-density three-dimensional localization microscopy across large volumes. Nat Methods 13, 359–365.

Lillemeier BF, Mortelmaier MA, Forstner MB, Huppa JB, Groves JT, Davis MM (2010). TCR and Lat are expressed on separate protein islands on T cell membranes and concatenate during activation. Nat Immunol 11, 90–96.

Mortensen KI, Churchman LS, Spudich JA, Flyvbjerg H (2010). Optimized localization analysis for single-molecule tracking and super-resolution microscopy. Nat Methods 7, 377–381.

Nanguneri S, Flottmann B, Horstmann H, Heilemann M, Kuner T (2012). Three-dimensional, tomographic super-resolution fluorescence imaging of serially sectioned thick samples. PLoS One 7, e38098.

Olivier N, Keller D, Gonczy P, Manley S (2013). Resolution doubling in 3D-STORM imaging through improved buffers. PLoS One 8, e69004.

Ovesny M, Krizek P, Borkovec J, Svindrych Z, Hagen GM (2014). ThunderSTORM: a comprehensive ImageJ plug-in for PALM and STORM data analysis and super-resolution imaging. Bioinformatics 30, 2389–2390.

Pertsinidis A, Mukherjee K, Sharma M, Pang ZP, Park SR, Zhang Y, Brunger AT, Sudhof TC, Chu S (2013). Ultrahigh-resolution imaging reveals formation of neuronal SNARE/Munc18 complexes in situ. Proc Natl Acad Sci USA 110, E2812–E2820.

Pertsinidis A, Zhang Y, Chu S (2010). Subnanometre single-molecule localization, registration and distance measurements. Nature 466, 647–651.

Rieger B, Stallinga S (2014). The lateral and axial localization uncertainty in super-resolution light microscopy. Chemphyschem 15, 664–670.

Rouquette-Jazdanian AK, Kortum RL, Li W, Merrill RK, Nguyen PH, Samelson LE, Sommers CL (2015). miR-155 controls lymphoproliferation in LAT mutant mice by restraining T-cell apoptosis via SHIP-1/mTOR and PAK1/FOXO3/BIM pathways. PLoS One 10, e0131823.

Rust MJ, Bates M, Zhuang X (2006). Sub-diffraction-limit imaging by stochastic optical reconstruction microscopy (STORM). Nat Methods 3, 793–795.

Schubert W, Bonnekoh B, Pommer AJ, Philipsen L, Bockelmann R, Malykh Y, Gollnick H, Friedenberger M, Bode M, Dress AW (2006). Analyzing proteome topology and function by automated multidimensional fluorescence microscopy. Nat Biotechnol 24, 1270–1278.

Sengupta P, Jovanovic-Talisman T, Lippincott-Schwartz J (2013). Quantifying spatial organization in point-localization superresolution images using pair correlation analysis. Nat Protoc 8, 345–354.

Sengupta P, Jovanovic-Talisman T, Skoko D, Renz M, Veatch SL, Lippincott-Schwartz J (2011). Probing protein heterogeneity in the plasma membrane using PALM and pair correlation analysis. Nat Methods 8, 969–975.

Sherman E, Barr V, Manley S, Patterson G, Balagopalan L, Akpan I, Regan CK, Merrill RK, Sommers CL, Lippincott-Schwartz J, *et al*. (2011). Functional nanoscale organization of signaling molecules downstream of the T cell antigen receptor. Immunity 35, 705–720.

Sherman E, Barr VA, Samelson LE (2013). Resolving multi-molecular protein interactions by photoactivated localization microscopy. Methods 59, 261–269.

Soares H, Henriques R, Sachse M, Ventimiglia L, Alonso MA, Zimmer C, Thoulouze MI, Alcover A (2013). Regulated vesicle fusion generates signaling nanoterritories that control T cell activation at the immunological synapse. J Exp Med 210, 2415–2433.

Sochacki KA, Shtengel G, van Engelenburg SB, Hess HF, Taraska JW (2014). Correlative super-resolution fluorescence and metal-replica transmission electron microscopy. Nat Methods 11, 305–308.

Stennett EM, Ciuba MA, Levitus M (2014). Photophysical processes in single molecule organic fluorescent probes. Chem Soc Rev 43, 1057–1075.

Szymborska A, de Marco A, Daigle N, Cordes VC, Briggs JA, Ellenberg J (2013). Nuclear pore scaffold structure analyzed by super-resolution microscopy and particle averaging. Science 341, 655–658.

Tam J, Cordier GA, Borbely JS, Sandoval Alvarez A, Lakadamyali M (2014). Cross-talk-free multi-color STORM imaging using a single fluorophore. PLoS One 9, e101772.

Thompson RE, Larson DR, Webb WW (2002). Precise nanometer localization analysis for individual fluorescent probes. Biophys J 82, 2775–2783.

Valley CC, Liu S, Lidke DS, Lidke KA (2015). Sequential superresolution imaging of multiple targets using a single fluorophore. PLoS One 10, e0123941.

van de Linde S, Loschberger A, Klein T, Heidbreder M, Wolter S, Heilemann M, Sauer M (2011). Direct stochastic optical reconstruction microscopy with standard fluorescent probes. Nat Protoc 6, 991–1009.

Wang S, Moffitt JR, Dempsey GT, Xie XS, Zhuang X (2014). Characterization and development of photoactivatable fluorescent proteins for single-molecule-based superresolution imaging. Proc Natl Acad Sci USA 111, 8452–8457.

Wiegand T, Moloney KA (2004). Rings, circles, and null-models for point pattern analysis in ecology. Oikos 104, 209–229.

Yi J, Wu X, Chung AH, Chen JK, Kapoor TM, Hammer JA (2013). Centrosome repositioning in T cells is biphasic and driven by microtubule end-on capture-shrinkage. J Cell Biol 202, 779–792.

Yi J, Wu XS, Crites T, Hammer JA 3rd (2012). Actin retrograde flow and actomyosin II arc contraction drive receptor cluster dynamics at the immunological synapse in Jurkat T cells. Mol Biol Cell 23, 834–852.